

Flexible Aqueous Li-Ion Battery with High Energy and Power Densities

Chongyin Yang, Xiao Ji, Xiulin Fan, Tao Gao, Liumin Suo, Fei Wang, Wei Sun, Ji Chen, Long Chen, Fudong Han, Ling Miao, Kang Xu, Konstantinos Gerasopoulos, and Chunsheng Wang*

A flexible and wearable aqueous symmetrical lithium-ion battery is developed using a single LiVPO_4F material as both cathode and anode in a “water-in-salt” gel polymer electrolyte. The symmetric lithium-ion chemistry exhibits high energy and power density and long cycle life, due to the formation of a robust solid electrolyte interphase consisting of $\text{Li}_2\text{CO}_3\text{-LiF}$, which enables fast Li-ion transport. Energy densities of 141 Wh kg^{-1} , power densities of $20\,600 \text{ W kg}^{-1}$, and output voltage of 2.4 V can be delivered during >4000 cycles, which is far superior to reported aqueous energy storage devices at the same power level. Moreover, the full cell shows unprecedented tolerance to mechanical stress such as bending and cutting, where it not only does not catastrophically fail, as most nonaqueous cells would, but also maintains cell performance and continues to operate in ambient environment, a unique feature apparently derived from the high stability of the “water-in-salt” gel polymer electrolyte.

Batteries with flexible configuration and conformability to be made into any shape as required would have wide applications in displays, wireless sensors, and implantable medical devices.^[1] To power these devices, the battery chemistry must be highly safe

when subjected to misshaping and deformation, nontoxic to the host where they are embedded, and stable with the ambient, in addition to the requirements for power, energy density, and cycling stability.^[2] The state-of-the-art Li-ion batteries (LIBs) deliver excellent power and energy performances, but the nonaqueous electrolytes used therein are highly flammable, toxic, and moisture-sensitive, thus constituting a high barrier to the flexibility of the LIB due to the necessary packaging and protective measures. As a result, there have been no real “flexible” LIBs till now, and the so-called flexible batteries on the market are still based on the same rigid form factor, with engineering solutions adopted at various levels, at the expense of energy densities and even safety, to cater the needs of unconventional form factors.^[3] These bat-

teries are neither flexible nor safe on the materials level; in fact, the attempts to make these LIBs flexible and stretchable seriously aggravate the already-existing safety concerns, the recent recall of Samsung Note 7 being the latest manifest.

To make a battery intrinsically safe, nontoxic, and flexible, the barrier imposed by nonaqueous electrolytes has to be removed. Aqueous electrolytes, which are nonflammable and environment-friendly, should provide an ideal solution, however their narrow electrochemical stability window (1.23 V) cannot accommodate the anode/cathode couples that provide high cell voltage and high energy density for LIBs. The low voltage ($<1.50 \text{ V}$) and energy density ($<70 \text{ Wh Kg}^{-1}$) of typical aqueous batteries make such efforts insignificant and irrelevant.^[4]

More recently, the new class of concentrated aqueous electrolytes, that is, “water-in-salt” (WiS) and “water-in-bisalt” (WiBS), successfully removed this last barrier to the fabrication of an intrinsically flexible and safe LIB. With their expanded electrochemical windows of $>3.0 \text{ V}$ enabled by a solid electrolyte interphase (SEI), their intrinsic nonflammability and moisture-insensitivity, as well as fast ion transport ($10^{-2} \text{ S cm}^{-1}$ at RT),^[5,6] these electrolytes already possessed all the elements to enable a high-rate flexible aqueous rechargeable Li-ion batteries (FARLBs), which should be able to assemble and operate in open air, because water molecules in both WiS and WiBS are strongly confined by salt coordination.


In this work, we constructed such a symmetrical FARLB based on a single Tavorite-type material LiVPO_4F as both anode

Dr. C. Yang, X. Ji, Dr. X. Fan, Dr. T. Gao, Dr. L. Suo, Dr. F. Wang, W. Sun, Dr. J. Chen, Dr. L. Chen, Dr. F. Han, Prof. C. Wang
Department of Chemical and Biomolecular Engineering
University of Maryland
College Park, MD 20740, USA
E-mail: cswang@umd.edu

Dr. L. Miao
School of Optical and Electronic Information
Huazhong University of Science and Technology
1037 Luoyu Road, Wuhan 430073, China

Dr. K. Xu
Electrochemistry Branch
Sensor and Electron Devices Directorate
Power and Energy Division
U.S. Army Research Laboratory
Adelphi, MD 20783, USA

Dr. K. Gerasopoulos
Research and Exploratory Development Department
Johns Hopkins University Applied Physics Laboratory
Laurel, MD 20723, USA

 The ORCID identification number(s) for the author(s) of this article can be found under <https://doi.org/10.1002/adma.201701972>.

DOI: 10.1002/adma.201701972

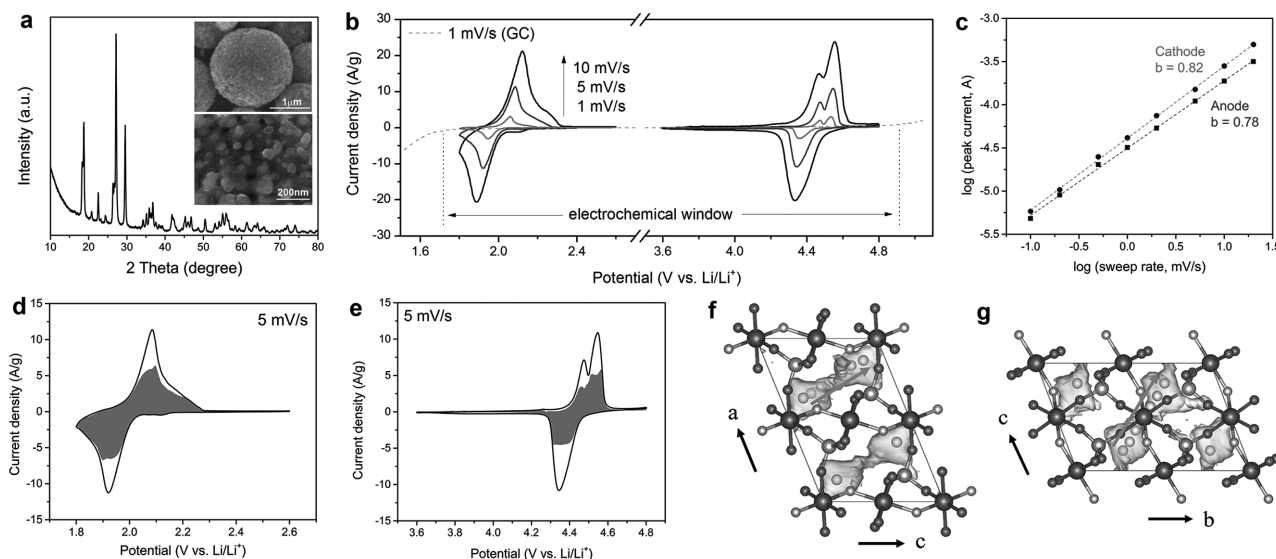


Figure 1. a) XRD patterns of as-synthesized LiVPO_4F samples. Inset: SEM images of as-synthesized LiVPO_4F particles (upper) and a close-up view of its surface (lower). b) Cyclic voltammograms (CV) of LiVPO_4F versus Ag/AgCl reference on both anode and cathode sides when scanned at 1–10 mV s^{-1} , wherein the potential has been converted to Li/Li^+ reference for convenience. The dashed CV loop of glassy carbon current collector shows overall electrochemical stability window. c) The $\log(i)$ versus $\log(v)$ plot of the peak current responses at ≈ 2.06 and ≈ 4.36 V (vs Li/Li^+). The slope of this line gives the b value for sweep rates (v) ranging from 0.1 to 20 mV s^{-1} . k_1 , k_2 analysis (Equation (3)) of LiVPO_4F on d) anode and e) cathode sides at 5 mV s^{-1} , respectively. f,g) bc and ac planes views of Li-ion probability densities obtained from AIMD simulations at 1573 K in LiVPO_4F . The 2D diffusion pathway along the b and c directions, as the green arrow illustrated. The Li, V, P, O, and F atoms are represented by green, big red, purple, small, and grey balls, respectively.

and cathode. The Li^+ -extraction/insertion of LiVPO_4F exhibited two distinct voltage plateaus, the upper one responsible for $\text{V}^{3+}/\text{V}^{4+}$ redox couple (≈ 4.26 V vs Li^+/Li), while the lower one for $\text{V}^{2+}/\text{V}^{3+}$ redox couple (≈ 1.8 V vs Li^+/Li).^[7,8] An output voltage of ≈ 2.46 V can thus be obtained from such a symmetric couple, which perfectly rests in the stability window of WiS electrolyte. Furthermore, a significantly enhanced power density is demonstrated in the aqueous electrolyte or its gel polymer form (GPE) because of the super-fast ion transport within LiVPO_4F and across its interphase and fast phase transformation.^[9,10] Besides ambient insensitivity and high safety, such cells also exhibit unprecedented tolerance against mechanical abuses such as bending and cutting, which neither terminate the cell nor cause any catastrophic outcome. To our best knowledge, this FARLB based on LiVPO_4F in WiS GPE is the first of its kind that is authentically flexible on materials level.

LiVPO_4F active material was prepared by two-step synthesis (see details in the Experimental Section). Figure 1a shows the X-ray diffraction (XRD) pattern for the as-synthesized material. All reflections can be indexed with a $\bar{P}1$ space group corresponding to pure LiVPO_4F tavorite-type structure, in good agreement with standard pattern of LiAlPO_4F (ICSD no. 48012).^[8] The obvious broadening of peaks usually indicate the nanosized crystalline grains.^[11] According to the well-known Scherrer formula

$$L = K\lambda/\beta\cos\theta \quad (1)$$

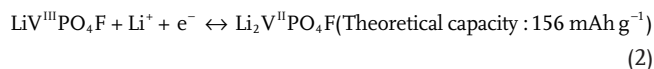
the average crystallite size, L , can be roughly estimated to be 67.9 nm. The scanning electron microscopy (SEM) in the inset of Figure 1a shows two levels of porous structure. The primary

sphere particles with microsized spheres of 1–2 μm in diameter consist of secondary carbon-coated nanoparticles with 50–100 nm in diameter. Nitrogen absorption/desorption isotherms showed a high Brunauer–Emmett–Teller (BET) specific surface area of 64.8 $\text{m}^2 \text{g}^{-1}$ and a major distribution of pore widths around 1–5 nm (Figure S1, Supporting Information). This structure effectively shortens the Li^+ diffusing distances and further accelerates redox reactions. This pomegranate-structured LiVPO_4F sphere takes advantages of both high energy density with large tapping density of microsized primary sphere and high power density of nanoscaled secondary carbon-coated LiVPO_4F where the highly electronic conductive 3D carbon matrix can further accelerate redox reactions of LiVPO_4F active material.

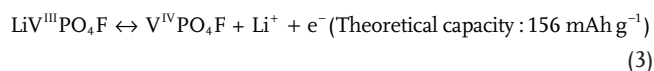
Prior to the fabrication of the flexible electrodes, electrochemical performance of LiVPO_4F in WiS GPE was investigated in a three-electrode cell using cyclic voltammetry (CV) at different scan rates from 0.1 to 20 mV/s . The LiVPO_4F electrode was prepared by dip-coating LiVPO_4F active material onto a glassy carbon current collector. WiS GPE was fabricated by dissolving 25 m lithium bis(trifluoromethane sulfonyl)imide (LiTFSI) salt in water at 90 $^\circ\text{C}$, where “m” stands for molality or mol-salt in kg-solvent, and then polyvinyl alcohol (PVA) with 1:1 mass ratio to water^[12] was dissolved into WiS to form transparent gel electrolyte without LiTFSI precipitation even at 25 $^\circ\text{C}$ (Figure S2, Supporting Information). Since LiTFSI solubility in water at 25 $^\circ\text{C}$ is only 21 m,^[6] this higher solubility of 25 m in the presence of PVA suggested that the PVA chains with abundant hydroxyl groups also participated in solvation, and must have interacted with the lithium salts. The Raman spectrum of WiS GPE is almost identical to that of the parental aqueous electrolyte (Figure S3, Supporting Information). It shows a high

ion conductivity of $\approx 9 \text{ mS cm}^{-1}$ at 25°C , which is also similar to aqueous WiS electrolyte and comparable to state-of-the-art nonaqueous electrolytes ($\approx 10 \text{ mS cm}^{-1}$).

Figure 1b shows the representative CV profiles of LiVPO_4F at difference scan rates from 1 to 10 mV s^{-1} (charging time from 10 to 1 min). At 1 mV s^{-1} , two pairs of redox peaks at 2.06 V/1.95 V and 4.53 V/4.36 V were clearly observed. The lower-potential pair corresponds to the reduction of V^{III} ($\text{V}^{\text{III}} \leftrightarrow \text{V}^{\text{II}}$)



While the higher potential pair should be attributed to the oxidation of V^{III} ($\text{V}^{\text{III}} \leftrightarrow \text{V}^{\text{IV}}$)



The split anodic peaks at 4.47 and 4.53 V are due to the occurrence of the $\text{Li}_{2/3}\text{VPO}_4\text{F}$ intermediate phase at a potential of 4.49 V with 1/3 of the charge.^[8] It should be noted that all the redox processes exhibited a positive shift of $\approx 0.2 \text{ V}$ compared with electrolytes with conventional salt concentrations,^[9] which has been attributed to the Li^+ activity change caused by the concentration electrolytes according to the Nernst equation.^[6] These two pairs of redox peaks at 2.06 V/1.95 V and 4.53 V/4.36 V reside well within the electrochemical stability window (1.7–4.9 V) of WiS GPE, which was evaluated using CV on a blank GC current collector (dashed loop in Figure 1b). The hydrogen evolution potential of 25 M WiS GPE shifted negatively from 1.92 V of 21 M WiS to 1.73 V. The anodic current at 5.2 V also significantly decreased by a factor of 4.5 (Figure S4, Supporting Information). The wider window of 25 M WiS GPE is expected from the higher lithium salt concentration in the gel WiS, which reduces free water and form more robust passivation SEI on anode side. Therefore, all the redox reactions of LiVPO_4F should proceed reversibly in WiS GPE.

The CVs at different scan rate provide further insight into the charge storage mechanism of LiVPO_4F . Figure 1c shows the plots of $\log(i)$ versus $\log(v)$ plot of the peak current responses at $\approx 2.06 \text{ V}$ on the anode side and at $\approx 4.36 \text{ V}$ on the cathode side (vs Li/Li^+). The current dependence on the sweep rate, v , is governed by the following relation^[10,13]

$$i = av^b \quad (4)$$

If the adjustable value of b is 0.5, the redox is controlled by a semi-infinite linear diffusion, indicating that Li -ions are stored inside LiVPO_4F , as they do in a battery. On the other hand, $b = 1$ indicates a capacitor-like nature where kinetics is surface-controlled. In aqueous electrolyte, LiVPO_4F exhibits values of b approximately between 0.78 and 0.82, implying that a significant portion of the Li^+ intercalation capacity has surface-controlled characteristics. Further analysis determines the level of this surface control reaction contribution by using the relation of current response, i , with a combination of capacitor-like and diffusion-controlled behaviors as follows^[13,14]

$$i = k_1v + k_2v^{1/2} \quad (5)$$

Both k_1 and k_2 can be determined using CV currents at different scan rates. Figure 1d,e showed the surface-control contributions to the total energy storage in the entire potential range. At a slow scan rate of 5 mV s^{-1} , surface-control contribution is 71% on the anode side and 75% on the cathode side. Therefore, a high power density device was enabled by the structure of LiVPO_4F that effectively shortens the Li^+ diffusing distances and further accelerates redox reactions.

The first-principle calculations indicated that rapid Li^+ diffusion is possible in the ac and bc plane of LiVPO_4F with low activation barriers. Figure 1f,g shows the projections on the ac and bc planes of a fast Li^+ diffusion path existing in the LiVPO_4F structure. The decomposed mean square displacement (MSD) profiles suggest that the major diffusion direction is along c -axis by b -axis (Figure S5, Supporting Information), with activation barrier of about 495 meV, which is comparable with that of spinel phase $\text{Li}_4\text{Ti}_5\text{O}_{12}$,^[15] a well-known high power density LIB anode material.

Besides the material-structure advantages of pomegranate LiVPO_4F , the fast reaction kinetics of LiVPO_4F and high ionic conductivity of WiS electrolyte ensure high power density of gel-WiS $\text{LiVPO}_4\text{F}/\text{LiVPO}_4\text{F}$ cell. In comparison, CVs of similar LiVPO_4F electrodes in 1 M LiPF_6 in EC/DMC electrolyte at different scan rate showed much higher polarization than those in WiS aqueous electrolyte (Figure S6a, Supporting Information). Further investigation of impedance profiles of the LiVPO_4F symmetrical cells revealed that WiS GPE provided much lower charge transfer resistance on the interphase (Figure S6b, Supporting Information).

The flexible electrode was prepared by doctor-blade casting a slurry of LiVPO_4F as active material, acetylene black (AB) as a conductive additive, and polyvinylidene fluoride (PVDF) as a binder on a titanium-coated flexible kapton film (details in the Experimental Section). The reaction thermodynamics and kinetics of the LiVPO_4F flexible electrode were evaluated in a three-electrode cell using galvanostatic intermittent titration experiments (GITT) (Figure 2a). After five initial activation cycles, a pulse current of 2 C was applied on LiVPO_4F electrodes for a short duration of 1 min, followed by 120 min relaxation at OCV to allow LiVPO_4F electrode to reach quasi-equilibrium (Experimental Section). The potential at the end of each relaxation stands for the quasi-equilibrium potential, while the potential difference between the potential at the end of each pulse (polarization potential) and the potential at the end of each relaxation (quasi-equilibrium potential) reflect the overpotentials. The reversible capacities ($\approx 145 \text{ mAh g}^{-1}$) of LiVPO_4F anode and LiVPO_4F cathode obtained using GITT is the maximum capacity which approaches the theoretical value of 156 mAh g^{-1} , and the best results achieved for LiVPO_4F .^[16,17] The overpotential of LiVPO_4F cathode is larger than that of LiVPO_4F anode, while both increase with state of charge/discharge due to increase in diffusion polarization. For LiVPO_4F cathode, the discharge overpotential (4 mV) is smaller than that during the charge, and it is comparable to the overpotential of LiVPO_4F anode, demonstrating high discharge rate capability of symmetric $\text{LiVPO}_4\text{F}/\text{LiVPO}_4\text{F}$ cell.

Since the single LiVPO_4F electrodes showed similar electrochemical capacities both on the anode and cathode sides, two identical LiVPO_4F electrodes are then used to construct

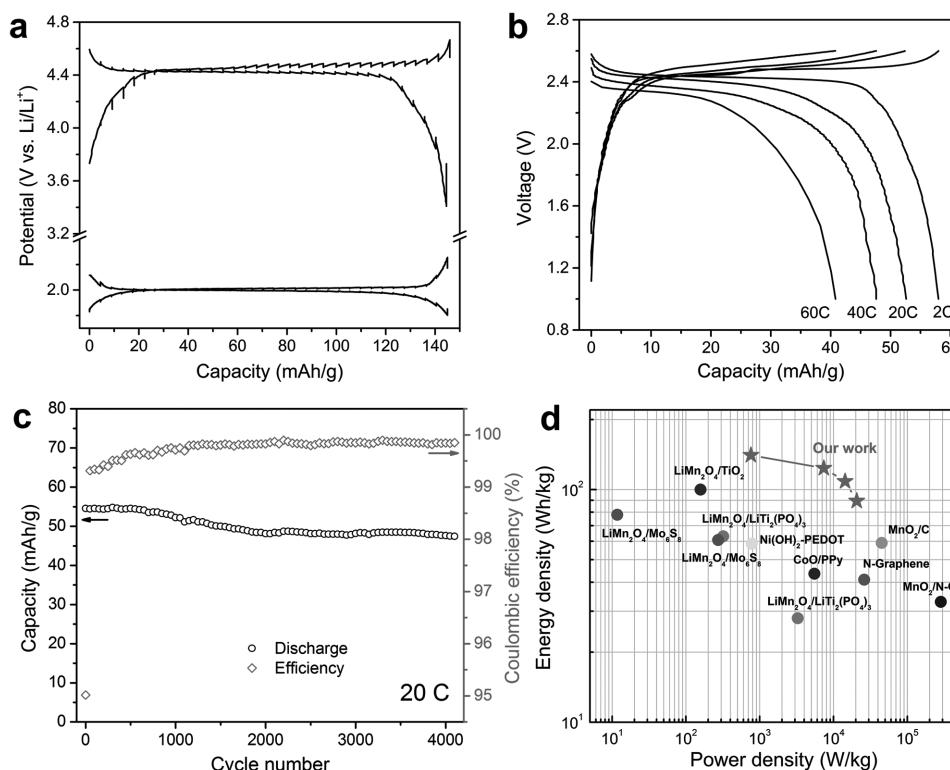


Figure 2. a) GITT characterization of LiVPO₄F versus Ag/AgCl reference on both anode and cathode sides at 2 C. The potential has been converted to Li/Li⁺ reference. The specific capacities were evaluated by active material mass. b) Charge and discharge voltage profiles of LiVPO₄F full cell at various rates (right to left: discharging at 2, 20, 40, and 60 C). c) Capacity retentions and coulombic efficiency of LiVPO₄F full cell at 20 C charge/discharge for 4000 cycles. The specific capacities were evaluated by total electrode mass. d) Ragone plot of LiVPO₄F full cell (red stars) in comparison with representative reported aqueous Li-ion batteries and supercapacitors (cycles). All the gravimetric capacities and energy densities are based on the total weight of positive and negative electrodes including the active materials, carbon additives, and binders (electrolyte and cell packaging were not considered).

a flexible belt-shaped symmetrical aqueous full cell using a thin layer of WiS GPE as electrolyte, which was prepared by a facile lamination process. Figure 2b shows charge/discharge behavior of symmetric LiVPO₄F/LiVPO₄F cell from 1 to 2.6 V at different C rates. The symmetric LiVPO₄F/LiVPO₄F full cell with a high LiVPO₄F loading ($\approx 5 \text{ mg cm}^{-2}$) and a low carbon black loading (5 wt%) showed superior rate capability. The achieved discharge capacity (based on total electrode mass) and average output voltage were 58.1 mAh g^{-1} (areal capacity: 0.58 mAh cm^{-2}) and 2.42 V at 2 C rate (0.314 A g^{-1}), 52.6 mAh g^{-1} and 2.35 V at 20 C (3.14 A g^{-1}), 47.6 mAh g^{-1} and 2.28 V at 40 C (6.28 A g^{-1}), 40.8 mAh g^{-1} and 2.19 V at 60 C (9.42 A g^{-1}), respectively. Such a high rate capacity (40.8 mAh g^{-1}) at 60 C is one of the best performance known in the battery electrode at the similar active materials and carbon loadings. Regardless of the increased current density, the polarization did not substantially increase at high discharge rates, which was in accordance with the negligible peak shifts in the CV results (Figure 1b). In addition to superior rate performances, the LiVPO₄F symmetric full cell also demonstrated excellent cycle life (Figure 2c), with 87% of initial capacity retained after 4000 cycles at 20 C at coulombic efficiency around 100%, which corresponds to a very small capacity decay of $0.003\% \text{ cycle}^{-1}$. Since the effect of side reactions is more pronounced at low C-rates, the cycling stability and coulombic efficiencies for 21 M WiS electrolyte and 25 M WiS GPE were compared at 0.2 C (Figure S7, Supporting

Information). As we mentioned, the wider electrochemistry window of 25 M WiS GPE enabled superior cycling stability at low rate of 0.2 C, accompanied by the coulombic efficiency approaching above 100% after only ten cycles. In contrast, the same LiVPO₄F/LiVPO₄F cell in 21 M WiS liquid electrolyte had a rapid capacity decay, with coulombic efficiency at only 96% after 50 cycles. The suppression of the side reactions was also confirmed by the extreme low self-discharge rate of a full cell (Figure S8, Supporting Information).

The Ragone plot (Figure 2d) compares the gravimetric power (P) and energy densities (E) of the LiVPO₄F full cell of this work with all reported values for aqueous Li-ion batteries and supercapacitors. The flexible symmetric LiVPO₄F full cell provides a specific energy of 141 Wh kg^{-1} and a specific power of 760 W kg^{-1} , which are both substantially higher than values reported for all other aqueous Li-ion batteries, such as $\text{Li}_{1.1}\text{Mn}_2\text{O}_4/\text{carbon-coated LiTi}_2(\text{PO}_4)_3$ (63 Wh kg^{-1}),^[18] $\text{LiMn}_2\text{O}_4/\text{Mo}_6\text{S}_8$ in WiS electrolyte (84 Wh kg^{-1}),^[6] $\text{LiMn}_2\text{O}_4/\text{carbon-coated TiO}_2$ in WiBS electrolyte (101 Wh kg^{-1}),^[5] and $\text{LiCoO}_2/\text{Li}_4\text{Ti}_5\text{O}_{12}$ (130 Wh kg^{-1}).^[19] At a high specific power of $20\,600 \text{ W kg}^{-1}$, the flexible LiVPO₄F cell can still deliver 90 Wh kg^{-1} of specific energy, which is much superior to most of the aqueous supercapacitors at the same power level, such as nitrogen-doped graphene (41 Wh kg^{-1} , 26 kW kg^{-1}),^[20] $\text{H-TiO}_2/\text{MnO}_2/\text{H-TiO}_2/\text{C NWs}$ (59 Wh kg^{-1} , 45 kW kg^{-1}),^[21] N-doped carbon/ MnO_2 (33 Wh kg^{-1} , 284 kW kg^{-1}),^[22]

CoO/PPy (43.5 Wh kg^{-1} , 5.5 kW kg^{-1}),^[23] and Ni(OH)₂-PEDOT (58.5 Wh kg^{-1} , 785 W kg^{-1}).^[24] The symmetric LiVPO₄F cell in WiS GPE beats both aqueous LIBs and aqueous supercapacitors with higher energy density and higher power density, respectively, due to its higher voltage 2.4 V and the unique pomegranate-structured LiVPO₄F. The resultant symmetric LiVPO₄F cell in WiS GPE can be considered as an intrinsically safe aqueous battery/supercapacity hybrid power device.

The mechanism for the superior performances of symmetric LiVPO₄F cell was investigated using XRD and X-ray photoelectron spectroscopic (XPS). Figure 3 shows the XRD and XPS spectra of the LiVPO₄F anode and cathode in the full cell after the 200th fully discharge and the 201st fully charge. The XRD spectrum of the LiVPO₄F/LiVPO₄F cell at the fully discharged charge state (i.e., LiVPO₄F anode at fully delithiated state and LiVPO₄F cathode at fully lithiated state) after 200 cycles is similar to that of the pristine material (Figure 1a), except for the LiF peaks on LiVPO₄F anodes. This indicates that LiVPO₄F maintains its original structure during long-term cycling. The LiF peaks that exist on cycled LiVPO₄F anode in both fully charged and discharged states after 200 cycles (Figure 3a, marked by stars) are attributed to LiF in SEI. However, in the fully charged state of the LiVPO₄F/LiVPO₄F cell, the indexes of the single-phase diffraction patterns of VPO₄F and Li₂VPO₄F appear. The two phases VPO₄F and Li₂VPO₄F in the fully charged state were refined in the more symmetrical space group C_{2/c},^[8] indicating

that both reactions ($\text{LiV}^{(\text{III})}\text{PO}_4\text{F} \rightarrow \text{V}^{(\text{IV})}\text{PO}_4\text{F}$ and $\text{LiV}^{(\text{III})}\text{PO}_4\text{F} \rightarrow \text{Li}_2\text{V}^{(\text{II})}\text{PO}_4\text{F}$) proceeded to completion during the full cell cycling, in accordance with the obtained capacities that are close to the theoretical values. The same chemical information is shown by XPS V 2p spectra (Figure 3b). For clarity, only the 2p_{3/2} component of the V 2p_{3/2}/2p_{1/2} doublet was analyzed. For the fully charged LiVPO₄F/LiVPO₄F cell, only V⁴⁺ (517.6 eV) on the surface of the fully charged VPO₄F cathode and V²⁺ (516.0 eV) on the fully discharged Li₂PO₄F anode were detected, while V³⁺ (516.6 eV) for LiVPO₄F is in complete absence.^[16,25]

A strong F 1s XPS peak at 685.7 eV (Figure 3c) corresponding to F⁻ in LiF was also detected, while a weak peak at 689.5 eV results from the PVDF binder in the composite electrode. These provided much clearer evidence that a LiF-rich SEI should have been formed from the electrolyte and covered the surface, serving as an electron barrier and preventing the reduction of water while allowing Li⁺ migration, than the ones demonstrated in our previous work.^[5,6] This SEI layer on the LiVPO₄F anode blocks the V signal (Figure S9, Supporting Information), which can only be exposed after Ar⁺ sputtering was conducted to remove SEI. In addition to LiF in SEI, an additional peak of O 1s at 528.3 eV corresponding to O²⁻ of certain oxide was also detected in the XPS O 1s (Figure 3c) besides the peak (531.4 eV) from the adsorptive O₂. Since the LiVPO₄F was covered by LiF-rich SEI, no O²⁻ signal origination from LiVPO₄F should be observed. Thus, the detected O²⁻ might be a

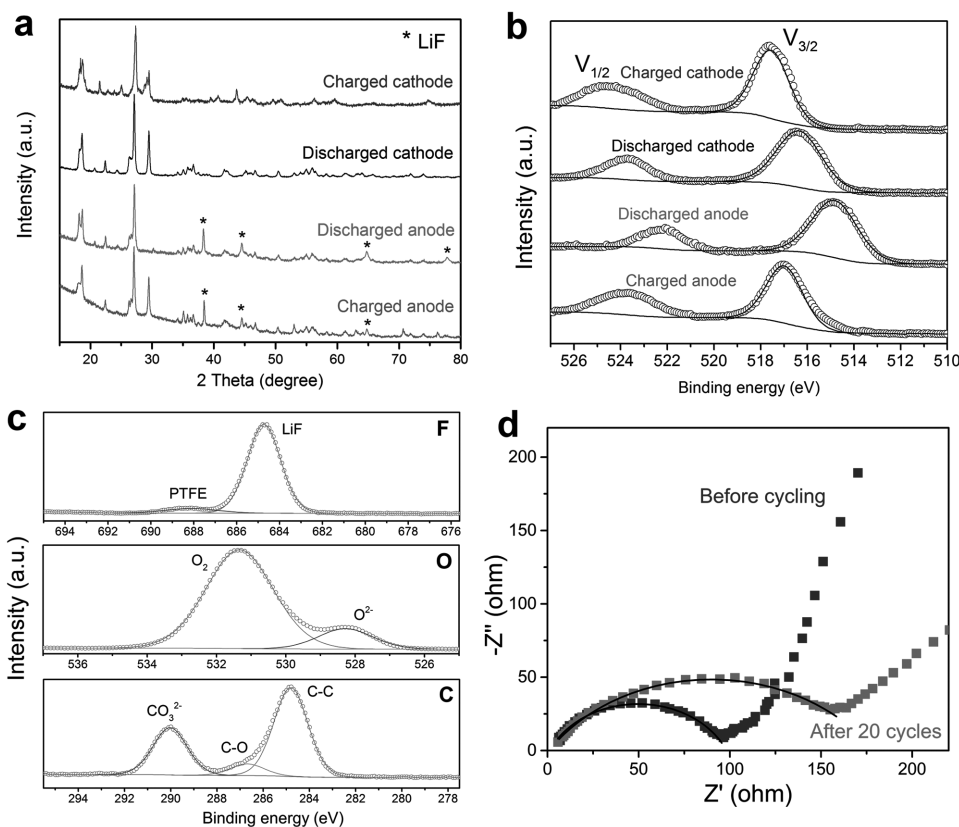


Figure 3. a) X-ray diffraction patterns and b) XPS V 2p spectra of the LiVPO₄F anode and cathode in full cell after 200th fully discharge and 201st fully charge. The XPS of anodes were etched by Ar⁺ sputtering to remove SEI layer. c) XPS F 1s, O 1s, and C 1s spectra of the LiVPO₄F fully discharged anode without Ar⁺ etching. d) Impedance profiles of the LiVPO₄F anode in a three-electrode cell before and after first 20 cycles in the frequency range of 100 mHz to 1 MHz. The black lines are their equivalent electrical circuit fittings.

component in SEI, which originates from the reduction of CO_2 in the aqueous electrolyte. Meanwhile, a strong peak of C 1s at 289.9 eV corresponding to CO_3^{2-} , which did not exist in the XPS spectra of the pristine electrode, was detected along with the ones corresponding to carbons in C–O or C–C linkages (286.7 and 284.8 eV) (Figure S10, Supporting Information).^[26] The atomic ratios of C from CO_3^{2-} peak, O from O^{2-} peak, F from F^- peak, and Li were calculated to be 3.21, 9.74, 6.53, and 12.65%, which were perfectly fitted to the SEI component formula of 49% Li_2CO_3 and 51% LiF. This is the first time that the SEI formed in aqueous electrolyte is found to be a mixture of Li_2CO_3 and LiF, whose ratio can be precisely determined. This finding in fact resolves a mystery about how Li^+ transport through an SEI if it is mainly based on LiF, with LiF being an insulator to either ionic or electronic conduction. Li_2CO_3 has a much better Li-ion conductivity than LiF;^[27] more importantly, according to Zhang et al., the space charge built up at the interfaces between LiF and Li_2CO_3 generates a region of higher carrier concentration than either bulk, which forms a channel for fast Li^+ transport.^[28] This Li^+ transport along LiF/ Li_2CO_3 grain boundary might be responsible for the high rate performances of LiVPO_4F anode even in the presence of a dense SEI. We measured the EIS of the anode in WiS GPE before and after the first 20 cycles in a three-electrode cell (Figure 3d). The

depressed semicircle is attributed to interfacial resistance. Its diameter increases after 20 charge/discharge cycles indicating the formation of SEI. However, the overall interface resistance increases by only 50%, demonstrating that a high Li-ion conductivity is still maintained across the LiF- Li_2CO_3 SEI.

The tolerance of LiVPO_4F -based FARLIB against mechanical abuses was tested while the cell is simultaneously subject to electrochemical cycling, and astonishing mechanical robustness and intrinsic safety of the symmetric LiVPO_4F cell was revealed. **Figure 4** shows the voltage profiles when the cells were bent at 90° and 180° , respectively, as well as when the cell was cut by half in the open air. Almost identical voltage profiles were recorded in the first two scenarios (Figure 4b). In further tests, the cell was bended for over 200 times, and the difference in capacities remains negligible (Figure S11, Supporting Information). In order to highlight the tolerance against abuse, a video (Video S1, Supporting Information) was filmed, in which a flexible cell with capacity of ≈ 60 mAh (2 C, Figure 4d) powers a mini-fan (requiring a power of ≈ 160 mW) while being cut in ambient air. In the video, the instantaneous short-circuit only results in a small energy loss, without catastrophic cell failure, while the strong bonding between H_2O and salt in WiS electrolyte prevents H_2O evaporation and ensures continuous operation of the gel-WiS electrolyte symmetric $\text{LiVPO}_4\text{F}/\text{LiVPO}_4\text{F}$ cell

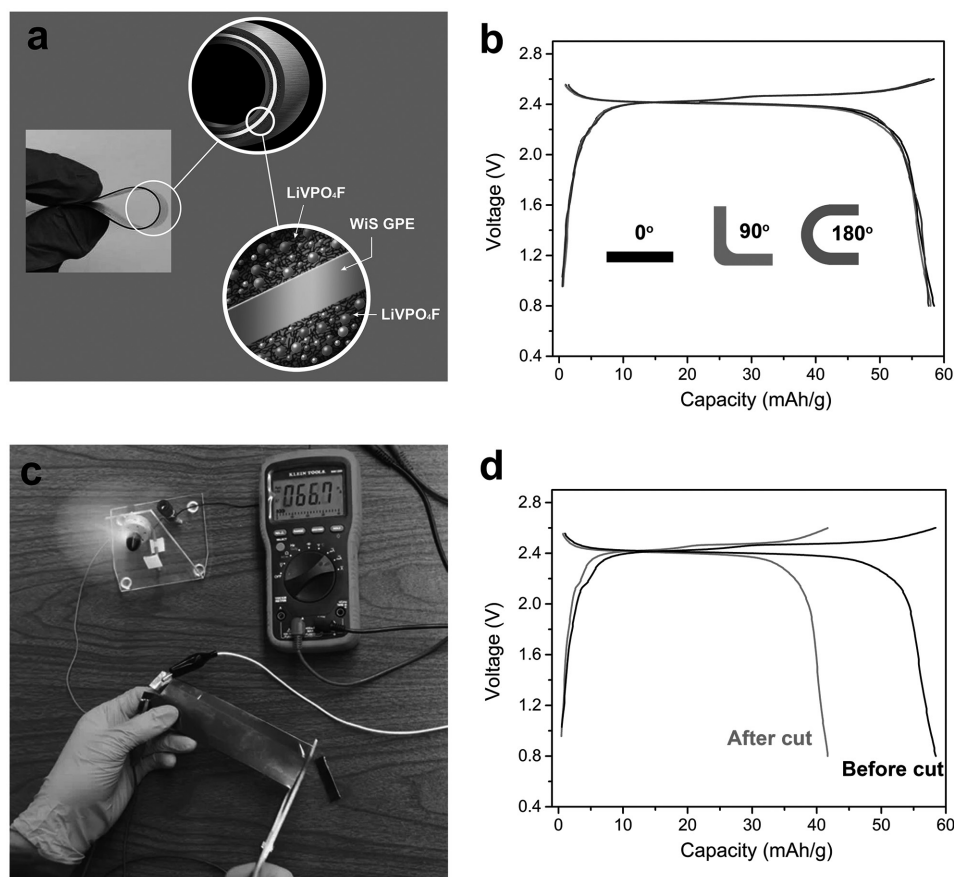


Figure 4. a) Fabricated flexible belt-shaped full cell and its mechanical flexibility. b) The voltage profiles of the flexible battery at 2 C under different bending angles: flat state, 90° and 180° bending, respectively; c) The robustness demonstration of aqueous flexible LiVPO_4F cell that powers an ≈ 160 mW while being cut in the open air. The reading of amperemeter is 66.7 mA. The cell survived cutting while continuing the operation in the open environment. d) The voltage profiles of the flexible battery at 2 C before and after being cut.

long after exposure to air. The most amazing part is that the cell can withstand cutting and continue to operate in an open cell condition without malfunction. To the best of our knowledge, this feature has not been previously reported for battery chemistries. The stability of the WiS electrolyte in the air was also confirmed by monitoring the weight retention of WiS GPE when exposing the electrolyte to air at room temperature for 20 d (Figure S12, Supporting Information). Instead of water loss, the electrolyte slightly gained weight during the first few hours, due to moisture extraction from the ambient (depending on the air humidity), after which the weight remains a constant. Hence, water evaporation in the open cell configuration is completely inhibited.

In summary, leveraging the advances of water-in-salt gel electrolytes and the two pairs of lithiation/delithiation redox reactions in LiVPO_4F , we created the first flexible, robust, and intrinsically safe LIB on materials level. Such a symmetric LiVPO_4F cell, while delivering superior energy (141 Wh Kg^{-1}) and power ($20\,600 \text{ W Kg}^{-1}$) densities and excellent cycling stability (>4000 cycles), can operate in open air, and exhibited unprecedented tolerance against mechanical abuses. This achievement opens the pathway for the first time to manufacturing LIBs at the site of need via 3D printing.

Experimental Section

Preparation of LiVPO_4F : The LiVPO_4F samples used in this study were all prepared using a two-step carbothermal reduction (CTR) method, which was described in previous work.^[29] Briefly, V_2O_5 (99.99%, Sigma-Aldrich), $(\text{NH}_4)_2\text{HPO}_4$ (99.99%, Sigma-Aldrich), and acetylene black were thoroughly mixed and heated at 750°C in flowing Ar atmosphere. A 20% mass excess of carbon was used to enable complete vanadium reduction and to ensure 5% of residual carbon in the product phase. The as-prepared intermediate product was further well mixed and reacted with LiF (99.99%, Sigma-Aldrich) to yield the final product in Ar at 650°C .

Preparation of Flexible Electrode and Electrolyte: The home-made flexible substrates were prepared by coating $75 \mu\text{m}$ thick kapton films with a Ti current collector ($0.5 \mu\text{m}$ thick) using e-beam evaporation. Electrodes were coated on the Ti surface with a weight-to-weight ratio of 85% of as-prepared LiVPO_4F sample, 5% carbon black, and 10% PVDF binder. The mass loading of electrode materials was $\approx 5 \text{ mg cm}^{-2}$. The aqueous gel electrolytes were prepared by dissolving 25 m (mol-salt in kg-solvent) LiTFSI ($>98\%$, TCI Co., Ltd.) and 10 wt% PVA (Sigma-Aldrich) in water (HPLC grade), which was similarly described in previous work.^[30] A homogeneous aqueous gel electrolyte formed at 95°C for 5 h under vigorous stirring.

Electrochemical Measurements: The three-electrode devices for cyclic voltammetry consist of LiVPO_4F dip-coated on glassy carbon film (2 in. \times 2 in.) as working electrode, active carbon (about 50 times the mass of the working electrode) as the counter electrode, and Ag/AgCl as the reference electrode. The GITT experiment was performed in a similar three-electrode device with flexible electrode as working electrode. The cycling protocol consists of 2 C current pulses for 1 min alternated with 120 min OCV periods. The flexible full cell was assembled by a facile lamination process using two identical electrodes with a thin layer of WiS GPE between them. After assembly, the cell was heated to 80°C for GPE self-healing. The cells were then cycled galvanostatically on a Land BT2000 battery test system (Wuhan, China) at room temperature.

Materials Characterizations: X-ray diffraction patterns were recorded on Bruker D8 Advance X-ray diffraction, with Cu K α radiation. SEM of the anode was performed in a Hitachi S-4700 operating at 5 kV. XPS analysis was performed with a high-resolution Kratos AXIS 165 X-ray

photoelectron spectrometer using monochromatic AlK α radiation. The ex situ tested electrodes were retrieved from the full cells, then soaked in acetone for 20 min to remove all remaining PVA and LiTFSI. The whole process was carried in pure Ar atmosphere to eliminate contamination. Pore size distributions, specific surface areas, and pore volumes of the samples were characterized by N_2 adsorption by means of a Micromeritics ASAP 2020 Porosimeter Test Station. Samples were degassed (in a vacuum) at 180°C for 12 h before the test. The specific surface areas were calculated using the BET method from the adsorption branch. The porosity distribution was calculated from adsorption branch using the BJH (Barrett–Joyner–Halenda) equation.

Supporting Information

Supporting Information is available from the Wiley Online Library or from the author.

Acknowledgements

The authors thank Dr. Junkai Hu for the help with the BET test. This work was supported by the U.S. Department of Energy ARPA-E (DEAR0000389) and the Johns Hopkins University Applied Physics Laboratory (JHU/APL) Independent Research and Development Program.

Conflict of Interest

The authors declare no conflict of interest.

Keywords

flexible battery, gel polymer electrolyte, rechargeable aqueous battery, water-in-salt

Received: April 9, 2017
Revised: August 30, 2017
Published online: October 16, 2017

- [1] a) X. Wang, X. Lu, B. Liu, D. Chen, Y. Tong, G. Shen, *Adv. Mater.* **2014**, 26, 4763; b) L. Li, Z. Wu, S. Yuan, X.-B. Zhang, *Energy Environ. Sci.* **2014**, 7, 2101.
- [2] a) J. M. Tarascon, M. Armand, *Nature* **2001**, 414, 359; b) N. S. Choi, Z. Chen, S. A. Freunberger, X. Ji, Y. K. Sun, K. Amine, G. Yushin, L. F. Nazar, J. Cho, P. G. Bruce, *Angew. Chem., Int. Ed. Engl.* **2012**, 51, 9994.
- [3] a) Y. H. Kwon, S.-W. Woo, H.-R. Jung, H. K. Yu, K. Kim, B. H. Oh, S. Ahn, S.-Y. Lee, S.-W. Song, J. Cho, H.-C. Shin, J. Y. Kim, *Adv. Mater.* **2012**, 24, 5192; b) N. Li, Z. Chen, W. Ren, F. Li, H.-M. Cheng, *Proc. Natl. Acad. Sci. USA* **2012**, 109, 17360; c) B. Liu, J. Zhang, X. Wang, G. Chen, D. Chen, C. Zhou, G. Shen, *Nano Lett.* **2012**, 12, 3005; d) K. T. Nam, D.-W. Kim, P. J. Yoo, C.-Y. Chiang, N. Meethong, P. T. Hammond, Y.-M. Chiang, A. M. Belcher, *Science* **2006**, 312, 885.
- [4] X. Dong, L. Chen, X. Su, Y. Wang, Y. Xia, *Angew. Chem. Int. Ed.* **2016**, 55, 7474.
- [5] L. Suo, O. Borodin, W. Sun, X. Fan, C. Yang, F. Wang, T. Gao, Z. Ma, M. Schroeder, A. von Cresce, S. M. Russell, M. Armand, A. Angell, K. Xu, C. Wang, *Angew. Chem., Int. Ed.* **2016**, 55, 7136.
- [6] L. Suo, O. Borodin, T. Gao, M. Olguin, J. Ho, X. Fan, C. Luo, C. Wang, K. Xu, *Science* **2015**, 350, 938.

- [7] B. L. Ellis, T. N. Ramesh, L. J. M. Davis, G. R. Goward, L. F. Nazar, *Chem. Mater.* **2011**, 23, 5138.
- [8] J.-M. Ateba Mba, C. Masquelier, E. Suard, L. Croguennec, *Chem. Mater.* **2012**, 24, 1223.
- [9] J. Barker, R. K. B. Gover, P. Burns, A. Bryan, *Electrochem. Solid-State Lett.* **2005**, 8, A285.
- [10] V. Augustyn, J. Come, M. A. Lowe, J. W. Kim, P. L. Taberna, S. H. Tolbert, H. D. Abruña, P. Simon, B. Dunn, *Nat. Mater.* **2013**, 12, 518.
- [11] V. Petkov, *Mater. Today* **2008**, 11, 28.
- [12] C. Wu, X. Lu, L. Peng, K. Xu, X. Peng, J. Huang, G. Yu, Y. Xie, *Nat. Commun.* **2013**, 4, 2431.
- [13] H. S. Kim, J. B. Cook, H. Lin, J. S. Ko, S. H. Tolbert, V. Ozolins, B. Dunn, *Nat. Mater.* **2017**, 16, 454.
- [14] J. W. Kim, V. Augustyn, B. Dunn, *Adv. Energy Mater.* **2012**, 2, 141.
- [15] B. Ziebarth, M. Klinsmann, T. Eckl, C. Elsässer, *Phys. Rev. B* **2014**, 89, 174301.
- [16] M. Kim, S. Lee, B. Kang, *Adv. Sci.* **2016**, 3, 1500366.
- [17] R. Ma, L. Shao, K. Wu, M. Shui, D. Wang, J. Pan, N. Long, Y. Ren, J. Shu, *ACS Appl. Mater. Interfaces* **2013**, 5, 8615.
- [18] V. Aravindan, Y.-S. Lee, S. Madhavi, *Adv. Energy Mater.* **2015**, 5, 1402225.
- [19] Y. Yamada, K. Usui, K. Sodeyama, S. Ko, Y. Tateyama, A. Yamada, *Nat. Energy* **2016**, 1, 16129.
- [20] T. Lin, I.-W. Chen, F. Liu, C. Yang, H. Bi, F. Xu, F. Huang, *Science* **2015**, 350, 1508.
- [21] X. Lu, M. Yu, G. Wang, T. Zhai, S. Xie, Y. Ling, Y. Tong, Y. Li, *Adv. Mater.* **2013**, 25, 267.
- [22] L. Chen, Z. Huang, H. Liang, Q. Guan, S. Yu, *Adv. Mater.* **2013**, 25, 4746.
- [23] C. Zhou, Y. Zhang, Y. Li, J. Liu, *Nano Lett.* **2013**, 13, 2078.
- [24] W. Jiang, D. Yu, Q. Zhang, K. Goh, L. Wei, Y. Yong, R. Jiang, J. Wei, Y. Chen, *Adv. Funct. Mater.* **2015**, 25, 1063.
- [25] G. Silversmit, D. Depla, H. Poelman, G. B. Marin, R. De Gryse, *J. Electron Spectrosc.* **2004**, 135, 167.
- [26] J. Contour, A. Salesse, M. Froment, M. Garreau, J. Thevenin, D. Warin, *J. Microsc. Spectrosc. Electron.* **1979**, 4, 483.
- [27] F. Ding, W. Xu, D. Choi, W. Wang, X. Li, M. H. Engelhard, X. Chen, Z. Yang, J.-G. Zhang, *J. Mater. Chem.* **2012**, 22, 12745.
- [28] Q. Zhang, J. Pan, P. Lu, Z. Liu, M. W. Verbrugge, B. W. Sheldon, Y.-T. Cheng, Y. Qi, X. Xiao, *Nano Lett.* **2016**, 16, 2011.
- [29] F. Zhou, X. Zhao, J. R. Dahn, *Electrochem. Commun.* **2009**, 11, 589.
- [30] C. Yang, L. Suo, O. Borodin, F. Wang, W. Sun, T. Gao, X. Fan, S. Hou, Z. Ma, K. Amine, K. Xu, C. Wang, *Proc. Natl. Acad. Sci. USA* **2017**, 114, 6197.